

# Multistatic Ground-Penetrating Radar Experiments

Tegan Counts, *Student Member, IEEE*, Ali Cafer Gurbuz, *Student Member, IEEE*,  
Waymond R. Scott, Jr., *Senior Member, IEEE*, James H. McClellan, *Fellow, IEEE*, and  
Kangwook Kim, *Member, IEEE*

**Abstract**—A multistatic ground-penetrating radar (GPR) system has been developed and used to measure the response of a number of targets to produce data for the investigation of multistatic inversion algorithms. The system consists of a linear array of resistive-vee antennas, microwave switches, a vector network analyzer, and a 3-D positioner, all under computer control. The array has two transmitters and four receivers which provide eight bistatic spacings from 12 to 96 cm in 12-cm increments. Buried targets are scanned with and without surface clutter, which is a layer of rocks whose spacing is empirically chosen to maximize the clutter effect. The measured responses are calibrated so that the direct coupling in the system is removed, and the signal reference point is located at the antenna drive point. Images are formed using a frequency-domain beamforming algorithm that compensates for the phase response of the antennas. Images of targets in air validate the system calibration and the imaging algorithm. Bistatic and multistatic images for the buried targets are very good, and they show the effectiveness of the system and processing.

**Index Terms**—Beamforming, ground-penetrating radar (GPR), measurement, multistatic radar, ultrawideband.

## I. INTRODUCTION

GROUND-PENETRATING radars (GPRs) image subsurface structures by transmitting short electromagnetic pulses into the ground and by receiving the reflections [1]. Considerable work has been performed on the development of the hardware and signal processing for these systems. Most of this work has been directed at monostatic systems or bistatic systems with closely spaced antennas. In this paper, we will investigate a multistatic system with eight different antenna spacings. We hypothesize that the multiple looks at a target from the variety of antenna spacings will make it easier to distinguish targets of interest from clutter. Other investigators have examined multistatic GPRs with varying degrees of success [2]–[4]. What makes this work different than the prior work is that measurements are made with the same system in three environments. This gives a range of environments to develop multistatic inversion algorithms. The targets are placed

in air for the first environment, which has a minimal uncertainty, and can be used to validate the performance of the algorithms in a known environment. The targets are buried in relatively homogeneous sand for the second environment; this scenario has more clutter and an unknown wave velocity that results in a more challenging inversion than the air environment. In the third environment, rocks are placed on the surface of the sand, which adds significant clutter, making the inversion much more difficult. Generally, clutter is the limiting factor for the performance of a GPR; therefore, the variety of clutter in the experiments should be useful in evaluating data processing algorithms.

A large variety of signal processing algorithms have been investigated. These can be divided into two categories: detection algorithms that attempt to detect specific sets of targets such as buried land mines or tunnels [5]–[8], and imaging algorithms that attempt to make an image of an underground region [2], [3], [9]–[13]. Back projection algorithms have proven to be relatively robust in imaging this type of data [2]. In this paper, we will present the results of our experiments using a frequency-domain imaging algorithm that is based on beamforming, which compensates for the phase response of the antennas as a function of both angle and frequency. The data are publicly available online at <http://users.ece.gatech.edu/~wrsconfig/> in Matlab format files. We believe that the data set can be a good starting point to prove the efficiency of multistatic inversion algorithms.

This paper is organized as follows. In Section II, the configuration of the multistatic GPR system and its data collection procedure are described. In Section III, the imaging algorithm is detailed. In Section IV, the experiments performed on targets suspended in air are described. Because air is a known and homogeneous medium, the inversion of the data obtained from the targets in air involves less uncertainties than the data obtained from the buried targets. Thus, the data described in Section IV can be used to calibrate the data obtained from the buried targets or to demonstrate the performance of multistatic inversion algorithms in a homogeneous medium. In Section V, the experiments performed on targets, which are buried in clean sand and in cluttered sand, are described.

## II. MULTISTATIC GPR

### A. System Description

The multistatic GPR in this paper consists of a linear array of resistive-vee antennas, a microwave switch matrix, a vector network analyzer (Agilent 8720D), and a 3-D positioner, all under computer control (Fig. 1). The resistive-vee antenna is

Manuscript received September 1, 2006; revised March 15, 2007. This work was supported in part by the U.S. Army Research Office under Contract DAAD19-02-1-0252.

T. Counts was with the School of Electrical and Computer Engineering, Georgia Institute of Technology, Atlanta, GA 30332-0250 USA. He is now with the Raytheon Company, Tucson, AZ 85706 USA.

A. C. Gurbuz, W. R. Scott, Jr., and J. H. McClellan are with the School of Electrical and Computer Engineering, Georgia Institute of Technology, Atlanta, GA 30332-0250 USA (e-mail: waymond.scott@ece.gatech.edu).

K. Kim is with the School of Information and Mechatronics, Gwangju Institute of Science and Technology, Gwangju 500-712, Korea (e-mail: mkkim@gist.ac.kr).

Color versions of one or more of the figures in this paper are available online at <http://ieeexplore.ieee.org>.

Digital Object Identifier 10.1109/TGRS.2007.900677

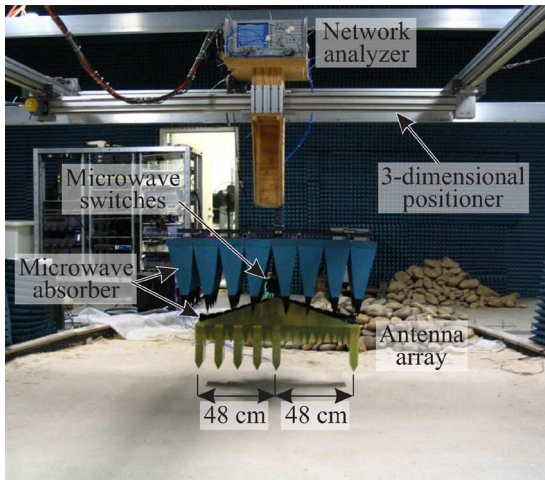


Fig. 1. Photograph of the experimental setup.

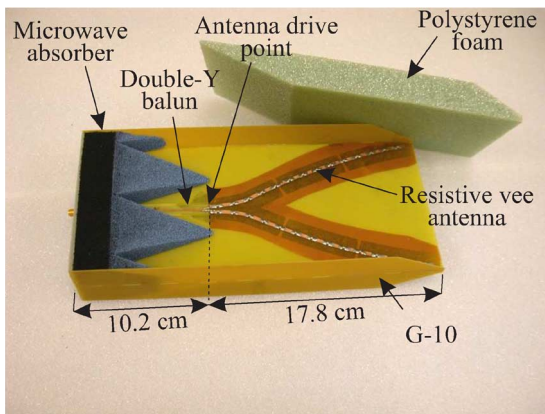


Fig. 2. Photograph of the resistive-vee antenna package. The resistive-vee antenna is supported by a G-10 frame. The space in the frame is filled with polystyrene foam, and the entire structure is encased with thin plastic film.

chosen as an array element because it can transmit and receive short pulses with a negligible amount of clutter, and it has a low radar cross section, which eliminates most of the multiple reflections between the antenna and the ground [14]–[16]. In addition, it is lightweight; therefore, an array of the resistive-vee antennas can be made in a hand-held form. The antenna was optimized for a bistatic GPR. To enhance the mechanical stability, the resistive-vee antenna is appropriately packaged [17] (see Fig. 2). The package includes a double-Y balun, which transforms a 50-Ω unbalanced line to a 200-Ω balanced line, and pieces of microwave absorber, which minimize the radar cross section of the package [18].

The antennas are housed in a nonmetallic frame, which can hold up to nine antennas with 12-cm spacing. In the current configuration, the array frame holds four receivers (R1, R2, R3, and R4) with 12-cm spacing and two transmitters (T1, T2) with 48-cm spacing (Fig. 3). These transmitters and receivers provide eight bistatic spacings from 12 to 96 cm in 12-cm increments.

The array frame is made up of 0.8-mm-thick G-10 material. The array frame has a larger radar cross section than the antennas, which can cause multiple reflections between the array frame and the ground. In order to lower the radar cross section

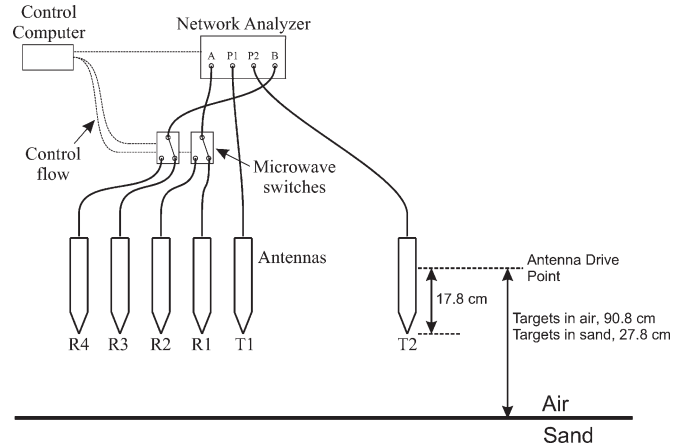


Fig. 3. Diagram of the multistatic GPR system and switching network.

of the array frame, pieces of 11.4-cm tall pyramidal microwave absorber are placed in the frame between the antennas. The microwave absorber is also used to wrap the cables from the antennas running behind the array frame. Wrapping the cables with the microwave absorber serves two purposes: one is hiding the electric conductors that are close to the antenna-target range, and the other is suppressing the common mode current on the cables, which is mostly caused by the imperfections of the balun used in the antenna. In addition, we used a 46-cm-tall pyramidal microwave absorber to prevent the reflections from the ground from reaching the positioner; this is important because waves reaching the positioner could reflect back toward the receiver in a way that cannot be easily removed.

The network analyzer has a single source and two samplers (i.e., A and B) [19]. The network analyzer is used to collect responses from eight bistatic pairs using one microwave switch inside the network analyzer and two external microwave switches, whose connections are computer-controlled, as shown schematically in Fig. 3. Transmitters T1 and T2 are directly connected to the network analyzer ports P1 and P2, respectively. The activation of T1 or T2 is determined by the state of the internal switch. Receivers R1 and R2 are connected to sampler A in the network analyzer through a microwave switch, and receivers R3 and R4 are connected to sampler B in the network analyzer through another microwave switch. Thus, the connection of either R1 or R2 to sampler A and the connection of either R3 or R4 to sampler B are determined by the states of the external switches.

The 3-D positioner holds the array frame and the network analyzer. It can move the GPR both horizontally and vertically. To minimize interference, the power, signal, and control cables run over the positioner. The signal cables from the network analyzer to the antenna and the control cables for the microwave switches are rigidly attached to the vertical post to minimize interference.

### B. Experimental Description

The GPR is scanned over a  $1.8 \times 1.8$  m region at a constant height above the surface of the ground. The scan region is referenced by  $x$ - and  $y$ -coordinates, both ranging from  $-90$  to  $90$  cm in 2-cm increments. Thus, the scan region is discretized

into a grid of 91 points by 91 points. The location of the GPR array in the coordinate system is referenced to the center point of transmitter T1. Each time the GPR array stops, it collects data from the eight bistatic spacings by manipulating switches in an appropriate order. After each switch operation, the network analyzer sweeps 401 equally spaced frequency points from 60 MHz to 8.06 GHz. This procedure at each point takes approximately 6 s. The total scan time is approximately 14 h.

The lowest effective frequency is in the range of 500 MHz–1.0 GHz because the gain of the antenna falls off quickly in this frequency range [20]. For the air targets, the high-frequency measurements are useful; however, for the buried targets, the upper useful frequency is limited by attenuation in the sand. The Fourier transform of a differentiated Gaussian pulse (4), which was centered at 2.5 GHz, was empirically chosen to window the subsurface data in the frequency domain. The measured frequency range was extended above and below the usable ranges to accommodate the frequency-domain window and provide additional data for other algorithms that may be able to exploit it.

The measured responses contain delays and attenuation in the signal cable, direct coupling between the antennas, etc. To eliminate these artifacts, a simple calibration procedure is applied. First, the antennas are removed from the array frame. Then, each transmitter–receiver port combination is connected by a 1.5-m-long cable, and the network analyzer measures the response through the cable,  $\text{THRU}(f, p)$ . Next, the antennas are mounted, and the network analyzer measures the bistatic responses in free space,  $\text{FREE}(f, p)$ . The free-space measurement is simulated by pointing the antenna toward the corner of the laboratory, which is covered with microwave absorber. Then, the measured data are calibrated as

$$\text{TR}(f, x_{\text{ant}}, y_{\text{ant}}, p) = \frac{\text{RAW}(f, x_{\text{ant}}, y_{\text{ant}}, p) - \text{FREE}(f, p)}{\text{THRU}(f, p)e^{-j2\pi ft_d}} \quad (1)$$

where  $p = 1, 2, \dots, 8$  are the eight bistatic pairs,  $f$  is the frequency,  $x_{\text{ant}}$  and  $y_{\text{ant}}$  are the coordinates of the array, and  $t_d$  is the combined delay through the 1.5-m-long cable and the transmitter and receiver baluns. The subtraction of FREE from the raw measurement eliminates the direct coupling between the antennas and the reflections from objects that are near the antenna array. The division by THRU eliminates the delay and attenuation in the signal cable. The division by  $e^{-j2\pi ft_d}$ , where  $t_d = t_{\text{cable}} - 2t_{\text{balun}}$ , removes both the effect of the 1.5-m thru cable and moves the phase reference from the connector at the end of the antenna package to the antenna drive point on the other side of the balun (see Fig. 2). Both  $t_{\text{cable}} = 7.27$  ns and  $t_{\text{balun}} = 580$  ps were measured experimentally.

The data calibrated according to (1) are stored in Matlab file format. Each Matlab file contains one set of measured and calibrated data obtained from a single scan of  $1.8 \times 1.8$  m region. The stored variables are responses from eight bistatic spacings ( $401 \times 91 \times 91$  double precision), frequency points at which the data are measured ( $401 \times 1$  double precision), and  $x$ - and  $y$ -coordinates of each measurement ( $91 \times 1$ ).

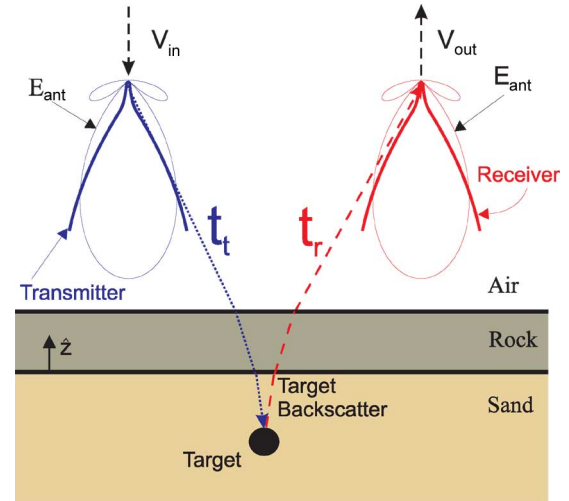


Fig. 4. Beamforming model. The propagation path from the transmitter to the target is the dotted line; object to receiver is the dashed line. Note that the radiation patterns in this figure are not the actual patterns (for actual patterns, see [20]).

### III. IMAGING ALGORITHM

The measured data have been imaged by a beamforming algorithm.

$$\text{Image}(x, y, z, p) = \sum_{x_{\text{ant}}} \sum_{y_{\text{ant}}} W(\bullet) \sum_f A(f) \times \frac{\text{TR}(f, x_{\text{ant}}, y_{\text{ant}}, p)}{e^{j\phi_{\text{trans}}(f, \bullet)} e^{-j\omega t_t(\bullet)} e^{-j\omega t_r(\bullet)} e^{j\phi_{\text{rcvr}}(f, \bullet)}} \quad (2)$$

Beamforming is the frequency-domain equivalent of the popular delay-sum backprojection algorithm [2]. This technique was chosen because it is straightforward, takes advantage of the synthetic aperture, and can easily and precisely account for the bistatic antenna spacings. The frequency-domain technique is preferred over the time-domain technique because it is easier to account for the phase response of the antennas as a function of frequency and look angle. The resistive-vee antenna has a phase response that is not accurately characterized as a constant phase center. The consequences of assuming a phase center are smearing of the images and significant perturbation of the vertical alignment of the bistatic images. This also affects the multistatic combination. In [21], a procedure is used to compensate for the phase response of the antennas as a function of frequency, and then the data are imaged. In [22], an experimental procedure is used to correct for the response of the antennas on boresight. In this paper, a procedure is used that compensates for the phase response as a function of both frequency and angle by modeling the antenna numerically in a method of moments code. Then, the code was used to calculate the far-field radiation pattern as a function of frequency and angle,  $E_{\text{ant}} = |E_{\text{ant}}|e^{j\phi_{\text{ant}}}$ . The phase angles  $\phi_{\text{trans}}$  and  $\phi_{\text{rcvr}}$  in (2) are the phases of the radiation pattern  $\phi_{\text{ant}}$  at the look angle of the propagation path (Fig. 4). These far-zone phase corrections have proven to be adequate for this work even though some of the targets are in the near-zone of the antennas.

The terms  $t_t$  and  $t_r$  in (2) and Fig. 4 are the travel times along the wave propagation path between the target and the transmitter/receiver. The travel times are dependent on the length of the propagation path and the propagation velocity in each medium. The travel paths are calculated based on a three-layer ground model [23]. A constant velocity is assumed in each layer:  $v_{\text{air}} = 2.998 \times 10^8$  m/s,  $v_{\text{sand}} = 1.50 \times 10^8$  m/s, and  $v_{\text{rock}} = 2.00 \times 10^8$  m/s. The rock and sand velocities were determined empirically using moveouts; the velocity was adjusted until the beamformed moveout of a buried target showed alignment across all pairs [24]. An approximation to Snell's law is used to determine the refraction points [23], [25]. For clean surface experiments,  $v_{\text{rock}}$  is set equal to  $v_{\text{air}}$ , effectively eliminating that layer from the model. Both  $v_{\text{rock}}$  and  $v_{\text{sand}}$  are set equal to  $v_{\text{air}}$  for the targets in air.

$W(\bullet)$  is an aperture weighting function

$$W(\bullet) = \sqrt{\frac{\cos(\theta_t) \cos(\theta_r)}{r_t r_r}} \quad (3)$$

where  $\theta_t$  and  $\theta_r$  are the polar angles between  $-\hat{z}$  and the rays from the transmitter and receiver to the image pixel. The frequency window  $A(f)$  is the Fourier transform of a differentiated Gaussian pulse

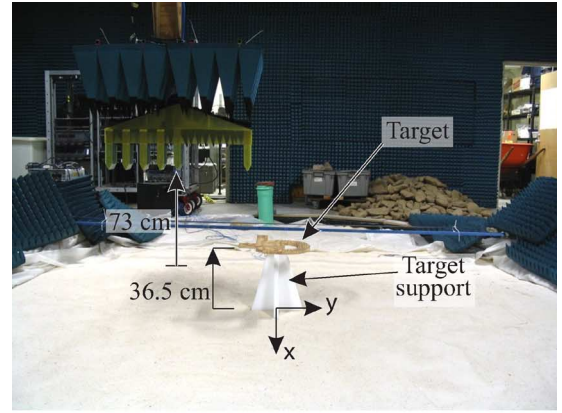
$$a(t) = V_0 \pi f_{\text{pk}} t e^{0.5 - 2(\pi f_{\text{pk}} t)^2} \quad (4)$$

where  $V_0 = 1$  is the peak-to-peak amplitude in the time domain, and  $f_{\text{pk}} = 2.5$  GHz is the peak frequency of the spectrum. The synthetic aperture is implemented by summing the contributions from many aperture locations  $(x_{\text{ant}}, y_{\text{ant}})$  to form each image pixel  $(x, y, z)$ . This will improve cross-range resolution. Range resolution is improved by summing over frequency. The  $(\bullet)$  represents a dependence on pixel location, antenna location, and pair number. Note that the values calculated for  $\text{Image}(x, y, z, p)$  are complex numbers. The real part of this image is what is normally obtained using the standard time-domain backprojection algorithm. The magnitude of the complex image can be viewed as the envelope of the standard time-domain backprojection algorithm; subsequent sections will all present magnitude images.

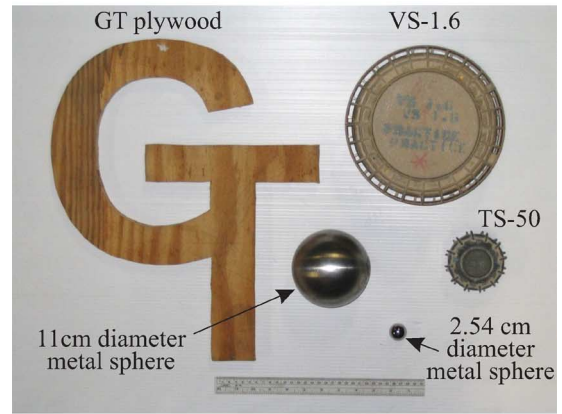
Initial results revealed a background layering in the images. This is due to variations in the coupling between cables that feed the antennas; the coupling changed between the free-space and full-scan measurements. The effect is low in frequency, highly regular, and independent of  $x$  and  $y$ ; therefore, it has been effectively taken out by subtracting the average of all vertical depth traces from each depth trace.

#### IV. MULTISTATIC GPR EXPERIMENTS FOR TARGETS IN AIR

The multistatic GPR is operated on targets in free space. Free space is simulated by elevating the targets to 36.5 cm above the surface of the ground and by scanning the array to 73 cm above the surface. Fig. 5 shows the photographs of the experimental setup and the targets used in the experiment. The targets are an 11-cm-diameter metal sphere, a 2.54-cm-



(a)



(b)

Fig. 5. (a) Photograph of the multistatic GPR experiment for targets in air and (b) photograph of the targets used in the experiment. A 30-cm-long ruler is shown in the target picture for scale.

TABLE I  
SUMMARY OF LANDMINE TARGET PROPERTIES

target	type	material	dimensions (cm)
VS-1.6	AT	plastic	22.2 (D), 9.2 (H)
VS-2.2	AT	plastic	24.0 (D), 12.0 (H)
TMA-5	AT	plastic	31.2 (L), 27.5 (W), 11.3 (H)
TS-50	AP	plastic	9.0 (D), 4.5 (H)
PFM-1	AP	plastic	11.9 (L), 6.4 (W), 2.0 (H)
M-14	AP	plastic	5.6 (D), 4.0 (H)
mine simulant	AP	plastic	7.5 (D), 3.8 (H)
sphere	clutter	aluminum	5.1 (D)
rock	clutter	rock	12.0 (L), 8.0 (W), 7.5 (H)
crushed can	clutter	aluminum	8.0 (D), 3.0 (H)
cylinder	clutter	nylon	15.5 (D), 7.6 (H)

diameter metal sphere, a VS-1.6 antitank (AT) mine, a TS-50 antipersonnel (AP) mine, and a  $38.5 \times 46.5 \times 1.8$  cm GT-shaped plywood. The properties of the mine targets are shown in Table I. The targets are placed on top of a polystyrene foam support, which is 54.3 cm below the antenna drive point.

Time-domain responses are obtained by transforming the calibrated frequency-domain response using the differentiated Gaussian input pulse defined in (4). Fig. 6 shows the time-domain response of the 11-cm sphere from each of the eight bistatic pairs. In each graph, the horizontal axis represents the

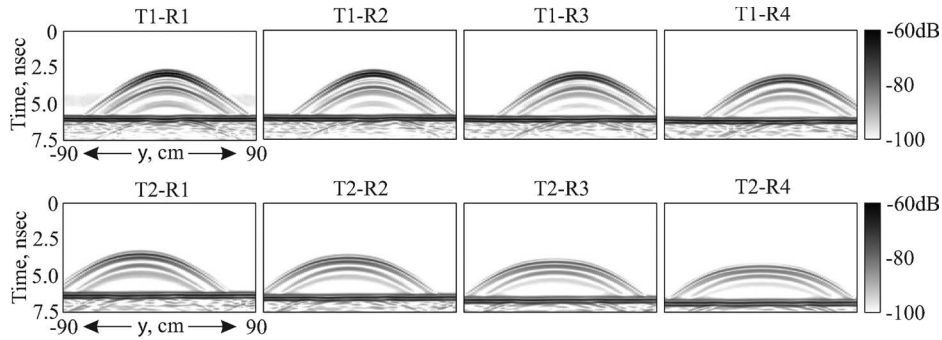


Fig. 6. Bistatic responses of the 11-cm-diameter metal sphere in air when the array is elevated by 73 cm and scanned over the line at  $x_{ant} = 0$ . Each is on a 40-dB scale.

$y$ -coordinates of the array, and the vertical axis represents the signal return time. The 2-D slices from this target at  $x_{ant} = 0$  are representative of the characteristics of all air targets; the response curves would have a hyperbolic shape for a monostatic antenna. Note that the peaks of the response curves appear at  $y_{ant} = 6, 12, 18,$  and  $24$  cm in the graphs for T1-R1, T1-R2, T1-R3, and T1-R4, respectively, and  $y_{ant} = -18, -12, -6,$  and  $0$  cm in the graphs for T2-R1, T2-R2, T2-R3, and T2-R4, respectively. The reason for this is that the  $y$ -coordinates in the graphs represent the center of the array, not the center of each bistatic pair. The peak of the response curve appears later in time as the transmitter–receiver spacing increases because the signal path length is longer for the wider bistatic pair. The intensity of the response curves is weaker for the wider bistatic pairs for the same reason. When targets are shallow, as they are in most experiments, the narrow pairs will have a significantly higher signal-to-noise ratio, and consequently, narrow pairs produce higher quality images. The strong horizontal responses, seen between 6.1 and 6.9 ns, are the reflections from the ground. Also in this figure, the responses of the metal sphere show a strong first peak followed by a weaker peak. The strong signal is the specularly reflected wave, and the weak signal is the creeping wave traveling around the sphere [26].

Beamformed images for selected air targets are shown in Figs. 7–10. The multistatic images in Figs. 7 and 10 are formed by summing the images of multiple pairs

$$Image'(x, y, z) = \sum_{p=1}^N Image(x, y, z, p) \quad (5)$$

and plotting the magnitude of  $Image'$  on a log scale. Each graph is normalized to the maximum magnitude image pixel in the entire 3-D space. Since the air targets are meant as a verification of the system in a simulated free space, the reflections from the ground were removed by time-gating. Vertical plane cuts through  $x = 0$  for the metal spheres and mines are shown in Fig. 7. The bottom of each target is at a depth of 54.3 cm below the antenna drive point. All of the targets and many target specific features are clearly visible. The 2.54-cm sphere looks like a point target. The 11-cm sphere shows a large response from the top of the target and a smaller response below the target that is due to the creeping wave. The image of the TS-50 shows reflections for the top and bottom of the mine.

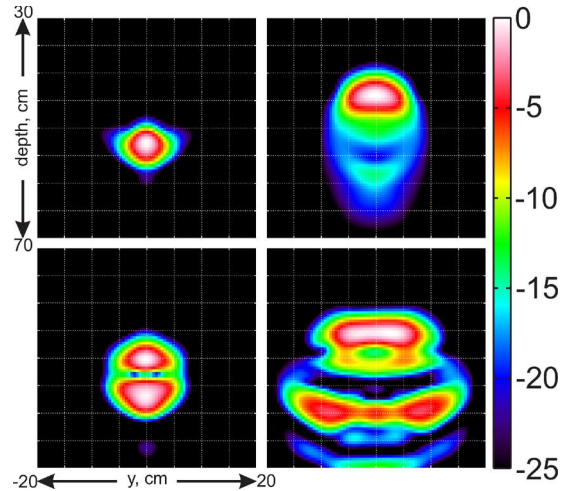


Fig. 7. Slice through  $x = 0$ . Targets are (clockwise starting top left) (a) 2.54-cm-diameter metal sphere, (b) 11-cm-diameter metal sphere, (c) VS-1.6 AT mine, and (d) TS-50 AP mine. Sum of four bistatic pairs. Each graph is normalized to its own maximum. Depth = 0 is at the antenna drive point.

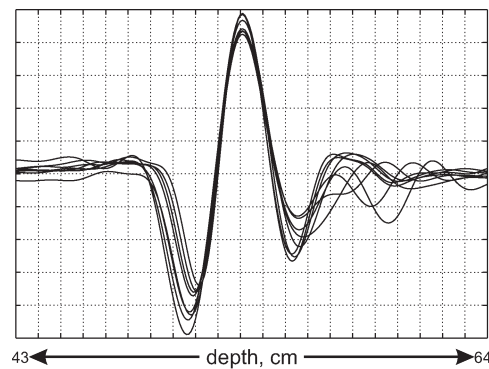


Fig. 8. One-dimensional depth trace through center of a 2.54-cm metal sphere in air. Real part of image data from all eight bistatic pairs versus depth. Each pair has been normalized by its maximum magnitude.

Reflections from the top and bottom of the VS-1.6 also give indications of the overall target shape. Below the VS-1.6 mine, there is a response at about  $-12$  dB that is almost certainly the result of multiple reflections within the mine.

Interpair alignment is critical when attempting to combine data from multiple bistatic pairs. This alignment was poor when using a standard time-domain backprojection because the method assumes a constant phase center that introduces errors.

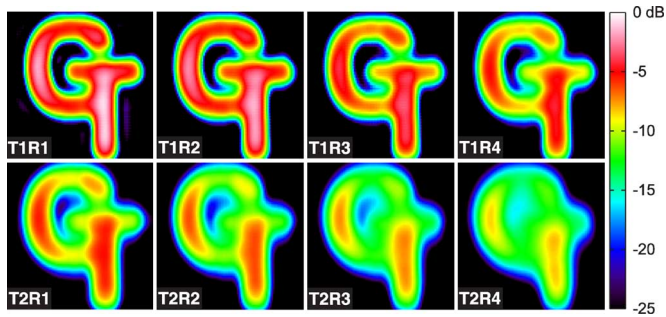


Fig. 9. Horizontal slice through the beamformed image of the GT sign for each of the eight bistatic pairs. Each figure has been normalized to the same global maximum. Images are 50-cm wide in both  $x$  and  $y$ . All graphs are on a 25-dB log scale.

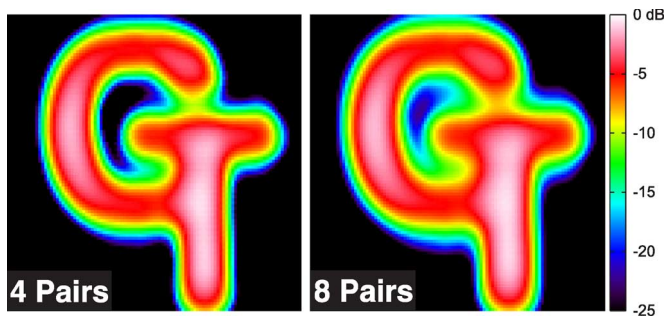


Fig. 10. Combination of four and eight multistatic pairs by addition. Each image has been normalized to its own maximum. Images are 50-cm wide in both  $x$  and  $y$ . All graphs are on a 25-dB log scale.

This prompted the conversion to frequency-domain beamforming along with the frequency-angle compensation of the phase response. To demonstrate the alignment between pairs, one depth trace through the center of the 2.54-cm sphere from each bistatic pair is drawn on the same graph (Fig. 8). Since complex numbers are being added to form a sum image (5), alignment of the real parts of the individual images is important. The alignment at the peak of the real part (which also is a zero of the imaginary part) is excellent. This verifies the physical measurements of the antenna dimensions, the accuracy of the time delay factors that make up  $t_d$  in (1), the numerical model of the antennas, and the ability of imaging algorithm to align the data.

Horizontal slices through the final air target, the plywood GT sign, show information about the cross-range resolution (Fig. 9). They clearly show the features in Fig. 5(b). The images are best for the narrow bistatic pairs; this can be explained by the fact that the beamwidth of the antenna decreases with increasing frequency. Patterns for the antenna have been previously documented [20]. Narrow beamwidths, particularly at high frequencies, and shallow targets (relative to bistatic spacings) combine to reduce the information on target (Fig. 11). As a result, the four widest pairs are unsuitable for the detection of shallow buried targets, but they are still useful for deeper targets [27]. Fig. 10 shows the coherent sums of the GT-shaped sign using four and eight bistatic pairs. The image with eight pairs is blurred by the wide pairs; this is expected since Fig. 11 indicates that a maximum of only six pairs should be considered.

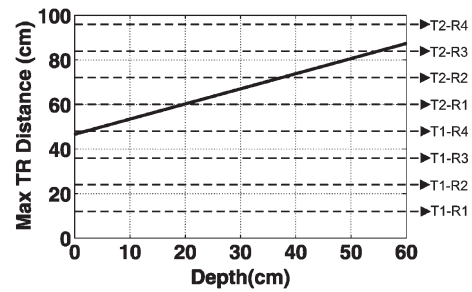


Fig. 11. Maximum transmitter–receiver spacing as a function of image pixel depth. For a given depth, only pairs below the line should be used. This restriction comes from the limited beamwidth only. Other factors also contribute to the inclusion of each pair.

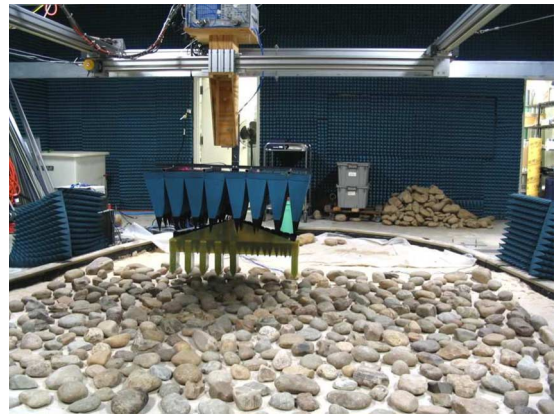


Fig. 12. Photograph of the multistatic GPR experiment for targets buried in sand with surface clutter.

## V. MULTISTATIC GPR EXPERIMENTS IN CLUTTERED ENVIRONMENT

The multistatic GPR is operated on five sets of buried targets. The target sets are an assortment of metal spheres, a variety of AT and AP landmines, a Plexiglas box, a plastic pipe, and empty sand. Table I contains more information about the landmine and clutter objects. Target depths range from 1 to 58 cm; the depth of a target is measured from the surface of the sand to the top of the target. The ground medium is damp compacted sand with a water table below target level.

Each set of targets is scanned with and without surface clutter according to the following procedure (the buried pipe is done only with a clean surface). First, the targets are buried, and the surface of the sand is packed so that the height of the surface varies less than 2 cm. The sand is then soaked with water and let stabilize for approximately 2 h. This process is performed to maintain appropriate moisture level in the sand and to minimize the disturbance made in the sand when the targets are buried. The responses of the targets in sand with a clean surface are obtained as the GPR scans over the sand. Next, river rocks are randomly scattered over the scan region, as shown in Fig. 12. The density of the rocks is empirically chosen to maximize the clutter effect. In both the clean-surface and cluttered-surface scans, the antenna array is elevated by 10 cm, which is measured from the surface of the sand to the bottom of the antenna array.

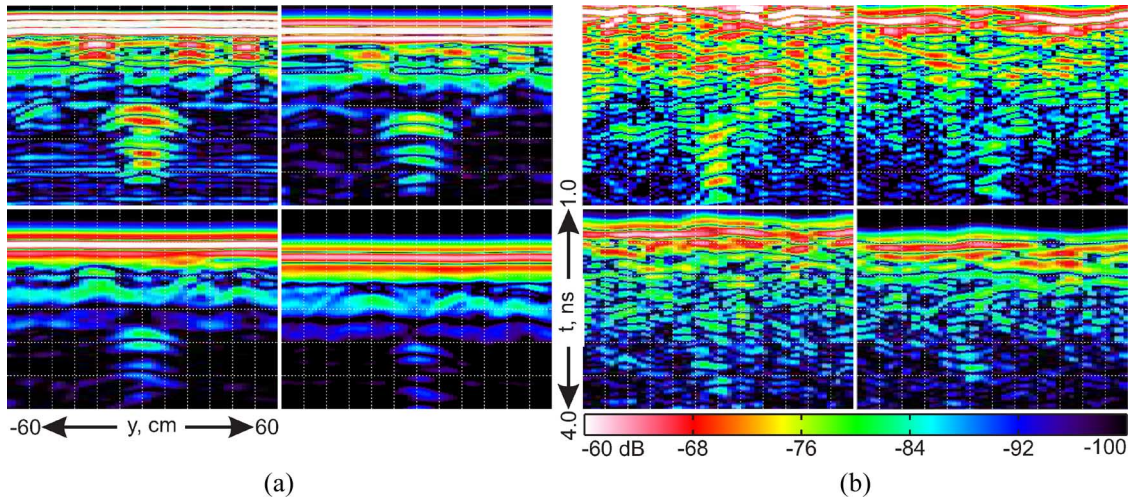


Fig. 13. Premigration bistatic landmine data in the time domain. (a) Clean surface. (b) Cluttered surface. Two-dimensional cut through the data at  $y = -40$  cm. Each image has a time (vertical) extent from 1–4 ns and a cross-range (horizontal) extent from  $-60$  to  $60$  cm. Pairs are (CW from top left) T1-R1, T1-R2, T1-R4, T1-R3.

When imaging the subsurface data to enhance the quality of the data for imaging purposes only, a ground deemphasis filter (6) has been applied to subsurface images

$$f(z) = z \left( \frac{1}{z + 0.10} \right). \tag{6}$$

The first term in (6) is the depth gain; the second term moderates the effect of the gain for deep targets; and the constant 0.10 in the denominator of the second term is to set the transition of the filter at 10 cm, which is a depth between the shallow and deep targets. For subsurface targets,  $z = 0$  is established at the air-ground interface. This type of filtering would most likely not be used by a detection algorithm, but it does improve the quality of the images by suppressing the clutter created by the air-ground interface. An alternative in dealing with the ground reflection is proposed by van der Merwe and Gupta [28].

The responses of the empty sand were taken, but they are not shown in this document due to space constraints. The raw data sets are available online with the data from all the other cases. The empty responses include subsurface clutter due to the variations of the sand and water densities. They may be useful in calibrating other data sets because they contain the same artifacts such as measurement errors, subsurface clutter, and the interactions between the ground and the radar. Similarly, the scenario containing buried metal spheres of various diameters is not presented in this paper.

### A. Landmines

Fig. 13 is calibrated data (1), windowed by (4), and transformed into the time domain. This is roughly the time-domain equivalent of the data input to the beamforming algorithm. Cuts at  $y = -40$  cm for the clean- and cluttered-surface experiments are shown for pairs T1-R1, T1-R2, T1-R3, and T1-R4. The burial map and target properties are shown in Fig. 15(b) and Table I, respectively. In Fig. 13(a), responses from four of five targets can be seen, but it is more difficult to distinguish

the small shallow targets from the surface response. It is not clear if any other targets are concealed by the clutter. The responses from the deeply buried targets, which are larger, show reflections from the tops and bottoms of the mines. As the bistatic spacing widens, shallow targets are even more obscured by the surface, but the deep targets are still visible despite the interference caused by the ground. Next, the calibrated target responses from the cluttered-surface experiment are obscured significantly by the rocks [Fig. 13(b)]. Shallow targets are difficult to identify, even for pair T1-R1, and they cannot be seen in the wider pairs. The deep targets can still be seen, but not as clearly.

Fig. 14 shows the results after applying the beamforming algorithm proposed in this paper. Each bistatic image is a plot of  $\text{Image}(x, 40 \text{ cm}, z, p)$  with the ground deemphasis filter (6) applied. The single multistatic image in each figure is  $\text{Image}'$  from (5) with (6) applied. All images have been normalized by the largest magnitude in their own 3-D image space. Beamformed images of the clean-surface data show that the target responses are almost completely separated from the ground disturbances. As expected, larger targets have stronger responses. The multistatic sum image is equivalent to or slightly better than the best single pair image, but the images are so good with one pair that there is not much room for improvement. More importantly, the additional pairs did not distort the image; this means that the interpair alignment is still good below the surface. Next, the beamforming is still effective in the cluttered surface case, but there are some targets that are missing. The deep targets and most of the shallow targets are seen distinctly, but one shallow target is not clearly distinguishable from the clutter ( $x = 45, y = -40$ ). The two targets (5.08-cm sphere, TS-50 at  $x = 45$  cm) that are difficult to detect in this 2-D slice are both enhanced by multistatic combination. Of the 12 targets under the heavy clutter in the entire 3-D space, eight of them form distinct patterns in the images. The multistatic combination technique is effective, yet it does not improve the images as much as expected. Perhaps the application of a more advanced algorithm would improve the results here.

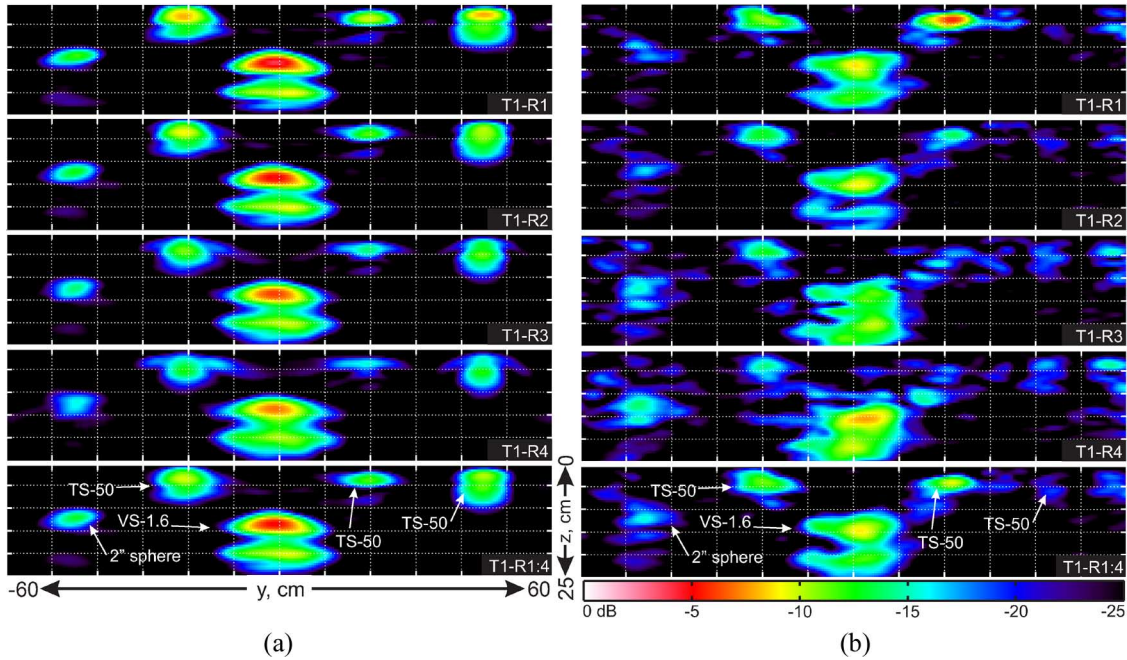


Fig. 14. Bistatic and multistatic images of landmines buried under both (a) clean and (b) cluttered surfaces. Two-dimensional cut through the data at  $y = -40$  cm. Each image has a depth extent from 0–25 cm and a cross-range (horizontal) extent from  $-60$  to  $60$  cm. Each pair is normalized to the maximum magnitude in its own 3-D image region.

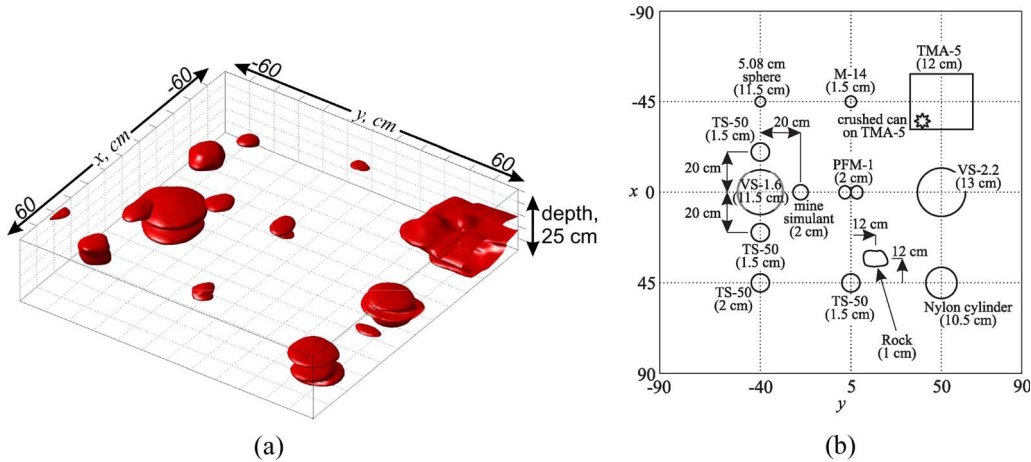


Fig. 15. (a) Three-dimensional iso-surface ( $-19$  dB) of the buried landmines with a clean surface. Four-pair combination. (b) Burial map of the targets.

Evaluating the quality of the GPR data is difficult in only two dimensions. Therefore, a 3-D iso-figure has been created to display information about the entire scan region for the clean surface landmine scenario. Fig. 15(a) is an iso-surface 19 dB down from the maximum of the region; this iso-level had been chosen empirically to maximize image quality. This image is a combination of the imaged data from the four narrowest bistatic pairs. The surface was not cluttered. All targets clearly appear, and there are only a few small speckles of clutter in the image.

**B. Buried Pipe**

A hollow plastic pipe was buried 58 cm deep in the same sand tank described above with the surface clear of rocks. The results of the beamforming algorithm and multistatic combination are shown in Fig. 16. Due to the greater depth of the pipe, all eight

bistatic pairs are used in the multistatic sum. Fig. 16 shows 2-D slices through the pipe. The clutter levels decrease with increasing bistatic antenna spacing, but the size of the target strong signature decreases too. The multistatic combination image has a reduced clutter level (when compared to the narrow pairs), yet it maintains a stronger target signature.

**VI. CONCLUSION**

A multistatic GPR system has been developed consisting of a linear array of eight resistive-vee antennas, microwave switches, a vector network analyzer, and a 3-D positioner, all under computer control. The GPR array provides eight bistatic pairs with spacings that range from 12–96 cm in 12-cm increments. The measured data are calibrated so that the direct coupling in the system and the cable effects are removed.

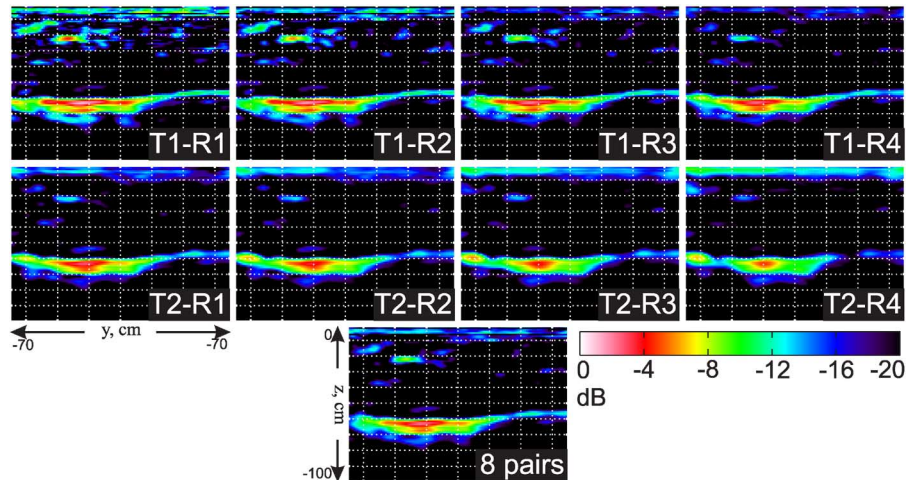


Fig. 16. Beamformed images of a tunnel buried at approximately 58 cm below the surface. Each image has a depth extent from 0–100 cm and a cross-range extent from  $-70$  to  $70$  cm. Each pair is normalized to the maximum magnitude in its own 3-D image region.

The calibrated data are stored and made available in the frequency domain in Matlab file format.

The GPR is operated on targets in air, which are two metal spheres, two landmines, and a GT-shaped plywood. The GPR is also operated on five sets of targets buried in sand with and without surface clutter. The target sets are empty sand, a Plexiglass box, a set of metal spheres, a set of landmines and clutter objects, and a pipe. The surface clutter is a layer of rocks scattered randomly over the scan region.

Images formed using the beamforming algorithm provide some insight into the quality of the data acquisition. Both 2-D and 3-D images of the data were presented. Coherently summing multiple bistatic pairs to form a single multistatic image has positive, although not profound, effects. This simple summing technique does show that there is some potential for more advanced multistatic GPR algorithms to produce results that are superior to bistatic acquisition.

In the future, this experiment might be improved by using antennas with a wider beamwidth over the entire frequency band. Widening the beamwidth would improve cross range resolution at the cost of reduced antenna gain and would allow more pairs to contribute to the image of shallow targets. Alternatively, tilting the antennas so that they all point more toward  $y = 0$  would increase the number of bistatic pairs that could contribute to the imaging of shallow targets. This would be at the expense of reducing the image swath width.

## REFERENCES

- [1] D. J. Daniels, Ed., *Ground Penetrating Radar*, 2nd ed. London, U.K.: Inst. Electr. Eng., 2004.
- [2] X. Feng and M. Sato, "Pre-stack migration applied to GPR for landmine detection," *Inv. Probl.*, vol. 20, no. 6, pp. S99–S115, Dec. 2004.
- [3] C. J. Leuschen and R. G. Plumb, "A matched-filter-based reverse-time migration algorithm for ground-penetrating radar data," *IEEE Trans. Geosci. Remote Sens.*, vol. 39, no. 5, pp. 929–936, May 2001.
- [4] C. Fischer, A. Herschlein, M. Younis, and W. Wiesbeck, "Detection of antipersonnel mines by using the factorization method on multistatic ground-penetrating radar measurements," *IEEE Trans. Geosci. Remote Sens.*, vol. 45, no. 1, pp. 85–92, Jan. 2007.
- [5] P. A. Torrione, C. S. Throckmorton, and L. M. Collins, "Performance of an adaptive feature-based processor for a wideband ground penetrating radar system," *IEEE Trans. Aerosp. Electron. Syst.*, vol. 42, no. 2, pp. 644–658, Apr. 2006.
- [6] P. Gader, M. Mystkowski, and Y. Zhao, "Landmine detection with ground penetrating radar using hidden Markov models," *IEEE Trans. Geosci. Remote Sens.*, vol. 39, no. 6, pp. 1131–1144, Jun. 2001.
- [7] A. Sullivan, R. Damarla, N. Geng, Y. Dong, and L. Carin, "Ultrawide-band synthetic aperture radar for detection of unexploded ordnance: Modeling and measurements," *IEEE Trans. Antennas Propag.*, vol. 48, no. 9, pp. 1306–1315, Sep. 2000.
- [8] T. G. Savelyev, L. van Kempen, H. Sahli, J. Sachs, and M. Sato, "Investigation of time-frequency features for GPR landmine discrimination," *IEEE Trans. Geosci. Remote Sens.*, vol. 45, no. 1, pp. 118–129, Jan. 2007.
- [9] L. Borcea, G. Papanicolaou, and H. Zhao, "Theory and applications of time reversal and interferometric imaging," *Inv. Probl.*, vol. 19, no. 6, pp. S134–S164, Dec. 2003.
- [10] L. Song and Q. H. Liu, "Ground-penetrating radar land mine imaging: Two-dimensional seismic migration and three-dimensional inverse scattering in layered media," *Radio Sci.*, vol. 40, 2005.
- [11] M. Rofheart and J. McCorkle, "Order  $N^2 \log(N)$  backprojector algorithm for focusing wide-angle wide-bandwidth arbitrary-motion synthetic aperture radar," in *Proc. SPIE—Radar Sensor Technology*, Jun. 1996, vol. 2747, pp. 25–36.
- [12] S. Oh, "Iterative space-time domain fast multiresolution SAR imaging algorithms," Ph.D. dissertation, Georgia Inst. Technol., Atlanta, GA, Nov. 2001.
- [13] C. Cafforio, C. Prati, and F. Rocca, "SAR data focusing using seismic migration techniques," *IEEE Trans. Aerosp. Electron. Syst.*, vol. 27, no. 2, pp. 194–207, Mar. 1991.
- [14] K. Kim and W. R. Scott, Jr., "Design and realization of a discretely loaded resistive vee dipole for ground-penetrating radars," *Radio Sci.*, vol. 39, no. 4, Jul. 2004.
- [15] K. Kim and W. R. Scott, Jr., "Design of a resistively-loaded vee dipole for ultra-wideband ground-penetrating radar applications," *IEEE Trans. Antennas Propag.*, vol. 53, no. 8, pp. 2525–2532, Aug. 2005.
- [16] T. P. Montoya and G. S. Smith, "Land mine detection using a ground-penetrating radar based on resistively loaded vee dipoles," *IEEE Trans. Antennas Propag.*, vol. 47, no. 12, pp. 1795–1806, Dec. 1999.
- [17] K. Kim and W. R. Scott, Jr., "Investigation of resistive vee antennas for a multi-static ground-penetrating radar," in *Proc. IEEE Antennas and Propag. Soc. Int. Symp.*, Jul. 3–8, 2005, vol. 3B, pp. 96–99.
- [18] J. B. Venkatesan and W. R. Scott, Jr., "Investigation of the double-Y balun for feeding pulsed antennas," in *Proc. SPIE—Detection and Remediation Technologies for Mines and Minelike Targets VIII*, Apr. 2003, vol. 5089, pp. 830–840.
- [19] Agilent Technologies, *Agilent 8719D, 8720D, and 8722D Network Analyzers Data Sheet*, 1998.
- [20] K. Kim and W. R. Scott, Jr., "A resistive linear antenna for ground-penetrating radars," in *Proc. SPIE—Detection and Remediation Technologies for Mines and Minelike Targets IX*, Apr. 2004, vol. 5415, pp. 359–370.

- [21] W. Clark, P. Lacko, J. Ralston, and E. Dieguez, "Wideband 3-D imaging radar using Archimedean spiral antennas," in *Proc. SPIE—Detection and Remediation Technologies for Mines and Minelike Targets VIII*, Apr. 2003, vol. 5089, pp. 167–178.
- [22] S. Lambot, E. Slob, I. van den Bosch, B. Stockbroeckx, and M. Vanclooster, "Modeling of ground-penetrating radar for accurate characterization of subsurface electric properties," *IEEE Trans. Geosci. Remote Sens.*, vol. 42, no. 11, pp. 2555–2568, Nov. 2004.
- [23] A. C. Gurbuz, T. Counts, K. Kim, J. McClellan, and W. R. Scott, Jr., "Application of multi-static inversion algorithms to landmine detection," in *Proc. SPIE—Detection and Remediation Technologies for Mines and Minelike Targets XI*, May 2006, vol. 6217, 621 724.
- [24] D. Leparoux, D. Gibert, and P. Cote, "Adaptation of prestack migration to multi-offset ground-penetrating radar data," *Geophys. Prospect.*, vol. 49, no. 3, pp. 374–386, May 2001.
- [25] E. Johansson and J. Mast, "Three dimensional ground penetrating radar imaging using a synthetic aperture time-domain focusing," in *Proc SPIE—Advanced Microwave and Millimeter Wave Detectors*, 1994, vol. 2275, pp. 205–214.
- [26] J. Rheinstein, "Backscatter from spheres: A short pulse view," *IEEE Trans. Antennas Propag.*, vol. 16, no. 1, pp. 89–97, Jan. 1968.
- [27] W. R. Scott, T. Counts, G. Larson, A. Gurbuz, and J. McClellan, "Combined ground penetrating radar and seismic system for detecting tunnels," in *Proc. Int. Geosci. Remote Sens. Symp.*, 2006, pp. 1232–1235.
- [28] A. van der Merwe and I. J. Gupta, "A novel signal processing technique for clutter reduction in GPR measurements of small, shallow land mines," *IEEE Trans. Geosci. Remote Sens.*, vol. 38, no. 6, pp. 2627–2637, Nov. 2000.



**Tegan Counts** (S'02) received the B.E.E. and M.S.E.E. degrees from the Georgia Institute of Technology, Atlanta, in 2006 and 2007, respectively.

From 2004 to 2007, he was a Research Assistant in the School of Electrical and Computer Engineering, Georgia Institute of Technology. He is currently with the Raytheon Company, Tucson, AZ. His research interest is investigating multistatic GPR techniques for detecting objects buried in the earth, including both antenna design and imaging algorithm development.

**Ali Cafer Gurbuz** (S'00), photograph and biography not available at the time of publication.



**Waymond R. Scott, Jr.** (S'81–M'82–SM'03) received the B.E.E., M.S.E.E., and Ph.D. degrees from the Georgia Institute of Technology, Atlanta, in 1980, 1982, and 1985, respectively.

In 1986, he joined the School of Electrical and Computer Engineering, Georgia Institute of Technology, as an Assistant Professor, where he was subsequently promoted to the rank of Professor. His research involves the interaction of electromagnetic and acoustic waves with materials. This research spans a broad range of topics, including the measurement of the properties of materials, experimental and numerical modeling, and systems for the detection of buried objects. His research is currently concentrated on investigating techniques for detecting objects buried in the earth. This work has many practical applications, for example, the detection of underground utilities, buried hazardous waste, buried structures, unexploded ordnance, and buried land mines.



**James H. McClellan** (S'69–M'74–SM'79–F'85) received the B.S. degree in electrical engineering from Louisiana State University, Baton Rouge, in 1969 and the M.S. and Ph.D. degrees from Rice University, Houston, TX, in 1972 and 1973, respectively.

Since 1987, he has been a Professor in the School of Electrical and Computer Engineering, Georgia Institute of Technology, where he is currently the John and Marilu McCarty Chair. He is a coauthor of *Number Theory in Digital Signal Processing*, *Computer Exercises for Signal Processing*, *DSP First: A Multimedia Approach*, and *Signal Processing First*, which received the McGraw-Hill Jacob Millman Award for an outstanding innovative textbook in 2003.

*A Multimedia Approach*, and *Signal Processing First*, which received the McGraw-Hill Jacob Millman Award for an outstanding innovative textbook in 2003.

Prof. McClellan was a corecipient of the IEEE Jack S. Kilby Signal Processing Medal in 2004.



**Kangwook Kim** (S'99–M'03) received the B.S. degree in electrical engineering from Ajou University, Suwon, Korea, in 1997 and the M.S. and Ph.D. degrees in electrical and computer engineering from the Georgia Institute of Technology, Atlanta, in 2001 and 2003, respectively.

From 1999 to 2003, he participated in the ultrawideband, pulse-radiating antenna research as a Graduate Research Assistant, and from 2003 to 2005, he participated in the multimodal landmine detection system research at the Georgia Institute of Technology as a Postdoctoral Fellow. From 2005 to 2006, he was with the Samsung Advanced Institute of Technology. He joined the School of Information and Mechatronics, Gwangju Institute of Science and Technology, Gwangju, Korea, as an Assistant Professor in 2006. His current research interests include electrically small antennas, sensing and imaging of concealed objects, and ultrawideband electromagnetics.